

Substitutional Alloying Using Crystal Graph Neural Networks

Dario Massa¹, Daniel Cieśliński¹, Amirhossein Naghdi¹
and Stefanos Papanikolaou^{1*}

^{1*}NOMATEN Centre of Excellence, National Centre for Nuclear
Research, ul. Andreja Sołtana 7, Otwock, Poland.

*Corresponding author(s). E-mail(s):
stefanos.papanikolaou@ncbj.gov.pl;

Abstract

Materials discovery, especially for applications that require extreme operating conditions, requires extensive testing that naturally limits the ability to inquire the wealth of possible compositions. Machine Learning (ML) has nowadays a well established role in facilitating this effort in systematic ways. The increasing amount of available accurate DFT data represents a solid basis upon which new ML models can be trained and tested. While conventional models rely on static descriptors, generally suitable for a limited class of systems, the flexibility of Graph Neural Networks (GNNs) allows for direct learning representations on graphs, such as the ones formed by crystals. We utilize crystal graph neural networks (CGNN) to predict crystal properties with DFT level accuracy, through graphs with encoding of the atomic (node/vertex), bond (edge), and global state attributes. In this work, we aim at testing the ability of the CGNN MegNet framework in predicting a number of properties of systems previously unseen from the model, obtained by adding a substitutional defect in bulk crystals that are included in the training set. We perform DFT validation to assess the accuracy in the prediction of formation energies and structural features (such as elastic moduli). Using CGNNs, one may identify promising paths in alloy discovery.

Keywords: GNN, CGNN, Graphs, Substitutional Alloys, Materials Discovery, Neural Networks, Machine Learning

1 Introduction

The use of machine learning (ML) [Michalski et al \(2013\)](#); [LeCun et al \(2015\)](#) methods in material science to accelerate materials discovery [Curtarolo et al \(2013\)](#) is at the base of the so-called material informatics (MI) [Ramakrishna et al \(2019\)](#); [Ramprasad et al \(2017\)](#); [Takahashi and Tanaka \(2016\)](#); [L. Ward \(2017\)](#); [Rajan \(2005\)](#). By training ML models on large databases, such as OQMD or the Materials Project high-throughput electronic structure calculation databases [Saal et al \(2013\)](#); [Jain et al \(2013\)](#); [Curtarolo \(2012\)](#); [Hachmann et al \(2011\)](#); NOMAD (<https://nomad-coe.eu>), the goal is to achieve predictions of material properties with quantum accuracy.

As in statistical mechanics with the need for identifying appropriate order parameters of novel phases and structures, the key challenge in ML algorithms is to identify effective system descriptors that can function as structure identifiers. A large variety of descriptors have been proposed, including fixed-length feature vectors of material elemental or electronic properties [Seko et al \(2015\)](#); [Xue et al \(2016\)](#); [Isayev et al \(2017\)](#), as well as structural descriptors, based on rotational and translational invariant transformations of atomic coordinates, like the Coulomb matrix [Rupp et al \(2012\)](#), atom-centered symmetry functions (ACSFs) [Behler \(2011\)](#), social permutation invariant coordinates (SPRINT) [Pietrucci and Andreoni \(2011\)](#), smooth overlap of atomic positions (SOAP) [De et al \(2016\)](#) and global minimum of root mean-square distance [Sadeghi et al \(2013\)](#). However, these solutions are often system-specific, and are not suitable for vast compositional and structural space exploration.

For this reason, a topic of fervent interest in the materials science community is the use of graph neural networks (GNNs) [Zhou et al \(2020\)](#); [Wu et al \(2021\)](#), which allow to learn representations directly and in a flexible way,

focused on molecular systems [Jorgensen et al \(2018\)](#); [Schütt et al \(2017\)](#); [Duvenaud et al \(2015\)](#); [Wu et al \(2018\)](#); [Kearnes et al \(2016\)](#); [Coley et al \(2017\)](#), surfaces [Back et al \(2019\)](#); [Palizhati et al \(2019\)](#); [Gu et al \(2020\)](#) and periodic crystals [Schütt et al \(2017\)](#); [Xie and Grossman \(2018a,b\)](#); [Chen et al \(2019a\)](#); [Dunn et al \(2020\)](#); [Louis et al \(2020a\)](#); [Park and Wolverton \(2020a\)](#); [Karamad et al \(2020\)](#); [Chen et al \(2019b\)](#). GNNs can be regarded as the generalization of convolutional neural networks (CNN) to graph-structured data, from which the internal materials representations can be learned and used for prediction of target properties [Reiser et al \(2022\)](#); even though larger amounts of data is required with respect to conventional ML models, GNNs take advantage of the unambiguous physics-guided real-space local associations between the system’s degrees of freedom, hence for any type of atomic crystalline structure [Gong and Yan \(2021\)](#). The common idea of GNN-based models is to represent atoms as nodes (V) and their chemical bonds as edges (E) in a graph $G(V,E)$, which can be fed to a trained neural network to create node-level embeddings (learned representations of each atom in its individual chemical environment) through convolutions with neighbouring nodes and edges [Fung et al \(2021\)](#). Therefore, given a set of learnable weights (W), and (y) a target material property, the GNN model reformulates the prediction task as the mapping $f(G : W) \rightarrow y$.

A direct benefit of the crystal material GNN-converted graph encoding is the naturally derived vector characterization of the atoms and edges [Louis et al \(2020b\)](#). The work of Xie *et al.* [Xie and Grossman \(2018a\)](#) represents the pioneering example of a crystal graph convolutional neural network (CGCNN) architecture, which has been later extended in the iCGCNN by Park *et al.* [Park and Wolverton \(2020b\)](#) to include 3-body correlations on neighbouring atoms, information on the Voronoi tassellated structure and an optimized chemical representation of interatomic bonds in the crystal graphs.

For the discovery of new materials, one may take various exploring paths, involving high-throughput computational [Curtarolo et al \(2013\)](#) and experimental [Liu et al \(2019\)](#) methods. However, the combined approach of machine-learning methods and compositional manipulation, has very quickly acquired a well established role in materials science, and it is applied in a wide range of property optimization searches like for zinc blende semiconductors [Mannodi-Kanakkithodi et al \(2022\)](#), perovskites [Zhai et al \(2022\)](#); [Balachandran et al \(2018\)](#); [Ye et al \(2018\)](#); [Sharma et al \(2020\)](#); [Klug et al \(2017\)](#); [Sampson et al \(2017\)](#) and others [Guan \(2019\)](#); [Ning et al \(2017\)](#); [Oba et al \(2018\)](#); [Deml et al \(2015, 2014\)](#); [Wan et al \(2021\)](#); [Varley et al \(2017\)](#); [Mannodi-Kanakkithodi et al \(2020\)](#).

In this work, we utilize a particular improvement of the originally proposed [Xie and Grossman \(2018a\)](#) CGCNN model, the MatERials Graph Network (MEGNet) model from Chen, Ye and coworkers [Chen et al \(2019b\)](#), introduced in [Sec.\(2.1.1\)](#), that has the merit of being developed and tested both on molecules and crystals, with the possibility of defining global state attributes including temperature, pressure and entropy. We test the capabilities of graph networks to predict the properties of single-atom substitutionally defected crystals with the MEGNet model. After considering a pre-trained model on the Materials Project (MP) database ([Sec.\(2.1.3\)](#)), we focus on the formation energies, bulk and shear moduli predictions, both comparing the results obtained in datasets of similarly defected structures ([Sec.\(3.1\)](#)) and the effects of almost all the possible single-atom defects in the same matrices ([Sec.\(3.2\)](#)). To validate the predictions, as described in [Sec.\(2.2\)](#) and [Sec.\(3.3\)](#), we perform Density Functional Theory (DFT) calculations, and we find CGNNs have both a great potential, but also limitations in predicting properties of defected bulk crystals, and promote materials discovery.

2 Methods

2.1 Machine Learning framework

2.1.1 MEGNet description

In the present work, we utilize the MEGNet model [Chen et al \(2019b\)](#). The reasons for this choice lie in the structure and performance of the model:

1. It is characterized by a low number of attributes, one for the atom (atomic number) and one for the bond (spatial distance), but MEGNet outperforms previous graph-based models [Chen et al \(2019b\)](#), as [CGCNN](#) [Xie and Grossman \(2018a\)](#) and [MPNN](#) [Jorgensen et al \(2018\)](#), with higher number of attributes, as well as [SchNet](#) [Schütt et al \(2017\)](#), with a similar low number.
2. the MEGNet framework includes a global state attribute, essential for state-property relationship predictions in materials,
3. The graph network construction of MEGNet has been developed and tested for both molecules and crystals

Here, we limit ourselves to present the main features of the model, but for a more exhaustive explanation we recommend the reader to the original work of [Chen et al.](#) [Chen et al \(2019b\)](#) and references there-in. In particular, given a graph $G(E, V, \mathbf{u})$, where

Parameter	Value	Short Description
nfeat_node	94	number of atom features
nfeat_global	2	number of state features
ngauss_centers	110	number of gaussians
converter_cutoff	4	cutoff radius
megnet_blocks	3	number of MEGNetLayer blocks
optimizer	Adam	optimizer of the model weights
lr	1e-3	learning rate
n1	64	number of hidden units in layer 1
n2	32	number of hidden units in layer 2
n3	16	number of hidden units in layer 3

Table 1: Parameters from the pre-trained MEGNet model.

- V is the set of N^v atomic attribute vectors \mathbf{v}_i ;
- $E = \left\{ (\mathbf{e}_k, \mathbf{r}_k, \mathbf{s}_k) \right\}_{k=1..N}^e$ is the set of N^e bond attribute vectors, with \mathbf{r}_k and \mathbf{s} being the indexes of the connected atoms;
- \mathbf{u} is the global state attribute vector;

the role of graph network is to recursively update a input graph $G(E, V, \mathbf{u})$ to an output graph $G(E', V', \mathbf{u}')$, with a progressive and inclusive information flow going from bonds to atoms, and finally to the global state. In particular, first the attributes of each bond are updated through a function ϕ_e , applied on the concatenation of the self-attributes, the ones of the connecting \mathbf{v}_{s_k} and \mathbf{v}_{r_k} atoms, and of the global state \mathbf{u} , as in

$$\mathbf{e}'_k = \phi_e(\mathbf{v}_{s_k} \oplus \mathbf{v}_{r_k} \oplus \mathbf{e}_k \oplus \mathbf{u}) \quad (1)$$

The update of atomic attributes involves the average over i -th atom connecting bonds $\bar{\mathbf{v}}_i^e = \frac{1}{N^e} \sum_{k=1}^{N^e} \{\mathbf{e}'_k\}_{r_k=i}$, the i -th atom self-attributes \mathbf{v}_i and the global state ones \mathbf{u} , as in

$$\mathbf{v}'_i = \phi_v(\bar{\mathbf{v}}_i^e \oplus \mathbf{v}_i \oplus \mathbf{u}) \quad (2)$$

Finally, an information flow from all three attribute groups is involved in the update of the global state attributes, as in

$$\mathbf{u}' = \phi_u(\bar{\mathbf{u}}^e \oplus \bar{\mathbf{u}}^v \oplus \mathbf{u}) \quad (3)$$

where $\bar{\mathbf{u}}^e = \frac{1}{N^e} \sum_{k=1}^{N^e} \{\mathbf{e}'_k\}$ and $\bar{\mathbf{u}}^v = \frac{1}{N^v} \sum_{i=1}^{N^v} \{\mathbf{v}'_i\}$.

As mentioned before, for our systems of interest, namely periodic crystals, the atomic number is the only node attribute. For bonds, the spatial distance

is expanded in a Gaussian basis set, centered at a linearly spaced r_0 locations between $r_0 = 0$ and $r_0 = r_{\text{cut}}$, and characterized by a given width σ ¹. Finally, the global state is simply a two zeros placeholder for global information exchange.

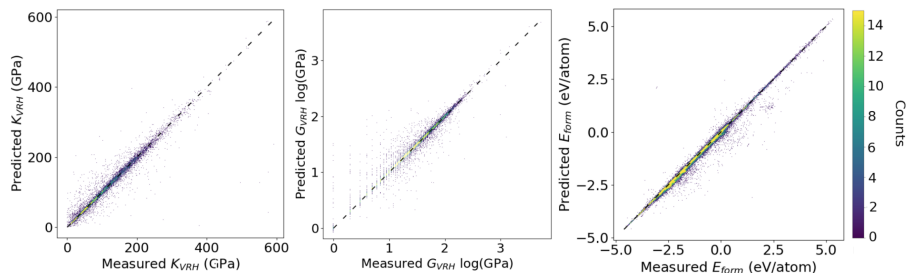


Fig. 1: Parity plots for the pre-trained model on the MP dataset. The plots involve the predictions on the bulk modulus (K_{VRH}), the shear modulus (G_{VRH}) and the formation energy (E_{form}).

2.1.2 Data collection

We consider crystal structures collected through the Python Materials Genomics interface (pymatgen) [Ong et al \(2013\)](#) to the Materials Application Programming Interface from Materials Project [Jain et al \(2013\)](#). When creating the dataset, there were 126301 structures in the database, that had formation energy (E_{form}) property, and 13102 structures that had bulk modulus (K_{VRH}) and shear modulus (G_{VRH}) properties.

2.1.3 Pre-trained model

Our focus in this work is on the prediction capabilities of MEGNet for *minimally* defected systems, that are clearly not in the training database, given the training of a dataset of undefected structures. In order to do so, we consider the substitution of a single atom in a supercell, hoping that CGNN

¹Therefore of shape $\exp(-(r - r_0)^2/\sigma^2)$.

training captures atomic similarities, based on combinations of atomic radii, valence electrons, and other atomic properties. Table(1) shows some of the parameters of the model, and a more complete list can be found at the default implementation of the class [Chen et al \(2022\)](#)

Property	MAE
K_{VRH}	6.143 GPa
G_{VRH}	10.489 GPa
E_{f}	0.029 eV/atom

Table 2: MAEs of the model for the prediction of the bulk modulus (K_{VRH}), shear modulus (G_{VRH}) and formation energy (E_{form}).

We report parity plots of Fig.(1) for all three properties of interest in this study: bulk modulus (K_{VRH}), shear modulus (G_{VRH}) and formation energy (E_{form}). To evaluate the model accuracy in predicting the properties of interest for the present study, the mean-absolute error (MAE) is used as the evaluation metric. Table(2) presents the MAE values for each predicted property over the dataset, which provides insights into the pre-trained model performance.

2.2 Validation with DFT

We verify the accuracy of the model’s predictions for system properties such as bulk modulus K_{VRH} , shear modulus G_{VRH} and formation energy E_{form} , after single-atom substitution is implemented in $2 \times 2 \times 2$ supercells. We perform DFT calculations with **Quantum Espresso** (QE) [Giannozzi et al \(2009, 2017, 2020\)](#) and its **THERMO_PW** [Dal Corso \(2023\)](#) driver for the calculation of structural properties. Pseudo-Potentials for all involved atomic species are Ultra-Soft and with Perdew-Burke-Ernzerhof (PBE) [Perdew et al \(1996\)](#) functional. The Methfessel-Paxton smearing [Methfessel and Paxton \(1989\)](#) has been introduced to correctly investigate metallic systems, and the calculations have been set as spin-polarized, for possible non-zero magnetization effects.

Convergence is checked on the number of k-points, plane-wave cutoff energy, and also, the energy smearing spreading (`degauss` parameter in QE), for each case, after a preliminary variable-cell relaxation of pure crystals, and then, further fixed-cell relaxation with optimal parameters, for final equilibrium bulk structures. The common acceptance threshold in the variation of the total energy upon parameter change is set at 10^{-5} Ry. Forces and total energy convergence thresholds for ionic minimization are set to a common value of 10^{-5} a.u. and 10^{-6} a.u. respectively. After optimization of pure crystals, fixed-cell relaxation is performed on supercells with single-atom substitutions, and its structural properties are then extracted through the `THERMO_PW` driver.

The computation of formation energies for validation purposes is performed on the case of single-atom substitutional defects (D) applied on pure bulk crystals (M), as follows,

$$E_{\text{form}}(\text{M}_{1-x}\text{D}_x) = E(\text{M}_{1-x}\text{D}_x) - (1-x)E(\text{M}) - xE(\text{D}) \quad (4)$$

where x is the atomic fraction of substitutional defects, $E(\text{M}_{1-x}\text{D}_x)$ is the total energy per atom of the compound, while $E(\text{M})$ and $E(\text{D})$ are the total energies per atom of the precursor species that compose it; the latter energies are obtained by relaxing the ground-state lattices of these species using the same aforementioned QE parameters as for the compound, as necessary to ensure computational consistency in the evaluation of accurate values for the defects formation energies.

3 Results: Property predictions for substitutional alloying with CGNN

There is a large variety of ways to systematically evaluate the effect of substitutional alloying on the properties of crystals [Kaxiras \(2003\)](#). Here, we focus on two key questions:

1. Data Science of Defects: What is the effect of substituting the same defect in a large variety of systems?
2. Is there qualitative and quantitative effects from atom-substituting various elemental defects in the same host crystalline matrix?

While it has not yet been possible to perform an exhaustive search of the kind, in this work, for the first part, the basin of host systems is represented by the Materials Project crystals dataset introduced in the previous sections [Jain et al \(2013\)](#), while for the latter part, the host systems are pure metallic bulk crystalline supercells of Al, Ni, Mo and Au.

3.1 An elemental defect seeing a wealth of different crystalline environments

First, we focus on the prediction of system properties, where the systematic substitutional defective process is applied using the same replacement atom, on randomly selected sites of crystals that exist in the the Materials Project crystals dataset [Jain et al \(2013\)](#). The aim is to explore how material properties change after single-atom substitution, evaluating deviations from original pure crystalline predictions, and how they depend on the specific substitution. For we consider three elemental cases: Rb, Mn and H, as the key replacement atoms that we will mutually compare. The reason for the choice lies in the drastic elemental differences among their unique characteristics and the assumption

	Weight(u)	Radius (pm)	El. Configuration
H	1.008	53	1s ¹
Mn	54.938	161	[Ar] 4s ² 3d ⁵
Rb	85.468	265	[Kr] 5s ¹

Table 3: Differences in the atomic properties of the three elements considered for the single-atom substitutional process. As an example, we report here the atomic weight, radius and electronic configuration.

that, on the base of these, we might be able to gain deeper understanding on how the model behaves in the predictions of previously unseen defect-induced changes in the system properties, basing on its learned notion of local environment. Table(3) reports, as an example, the values of the atomic weight, radius and electronic configuration of each considered replacement atom.

In Fig.(2), we display the predictions of MEGNet for the bulk moduli of Rb-defected systems with respect to the original, pure ones. As contained in Table(4), this kind of substitutional defect causes the largest root-mean-squared (RMSD) deviations among the three considered atomic species, with a value of approximately 6.2 GPa. In this section, we only report plots referring to the largest RMSD cases, but analogous plots can be found in the Appendix Sec.(A).

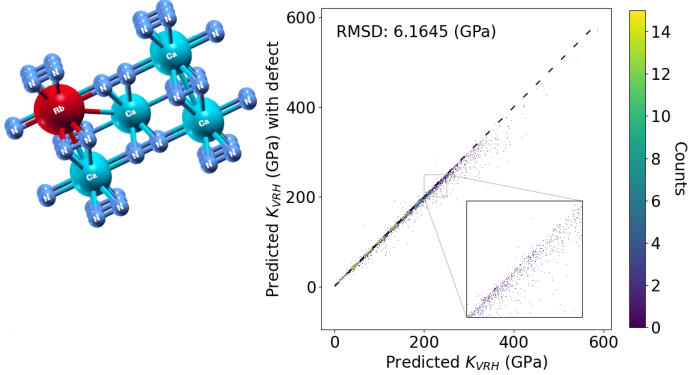


Fig. 2: Predicted bulk moduli in the Rb-defected MP crystals with respect to their prediction in non-defected ones. An example structure from the MP dataset is shown, CaN₂, in which one atom of Ca has been replaced with a Rb atom. Here only the case of Rb-defected systems is shown, due to its largest RMSD among the set of considered defects. Similar plots for the Mn- and H-defected systems are contained in the Supplementary Materials.

Defect	RMSD (GPa)
Rb	6.1645
Mn	3.1274
H	1.2975

Table 4: RMSD (GPa) for the prediction of the bulk modulus (K_{VRH}) in Rb, Mn, and H single-atom substitutionally defected systems with respect to the non-defected ones.

Also the shear moduli predictions show the largest RMSD for the case of a Rb-defect, with a value of $0.0628 \log(\text{GPa})^2$. The results are shown in Fig.(3) and on Table(5). According to the model, it seems that both K_{VRH} and G_{VRH} upon substitution of a Rb atom, are showing a tendency to decrease their value, respectively, implying an increase in their compressibility and decrease in hardness. It is worth noticing that even though the only physical atomic

²As it can be visible from an analogous plot in the Supplementary Material, without a log-log scale the deviations cannot be correctly estimated. This is the reason why we decided to report the G_{VRH} prediction plots and RMSD values in these units.

feature that the model exploits is the atomic number, the prediction of larger changes in the structural properties for involved defects with larger radii can be regarded as a reasonable one.

Defect	RMSD (log(GPa))
Rb	0.0628
Mn	0.0350
H	0.0435

Table 5: RMSD (log(GPa)) for the prediction of the shear modulus (G_{VRH}) in Rb, Mn, and H single-atom substitutionally defected systems with respect to the non-defected ones.

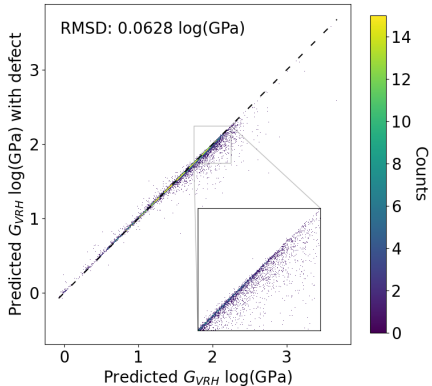


Fig. 3: Predicted shear modulus in the Rb-defected MP crystals with respect to the prediction in non-defected ones. Here only the case of Rb-defected systems is shown, due to its largest RMSD among the set of considered defects. Similar plots for the Mn and H-defected systems are contained in the Supplementary Materials.

Furthermore, in Fig.(4), we show the predicted deviations in the formation energy of the MP-defected samples for the case of elemental H, and also for all three elements in Tab.(6). As it can be seen, the deviations are all in the order of 0.02 eV/atom, and are progressively less prominent going from H, to Rb and Mn.

3.2 A crystalline matrix seeing a wealth of different elemental defects

The case of systematically changing the single-atom substitutional defect species in the same crystalline matrix is complementary to the prior addressed

Defect	RMSD (eV/atom)
Rb	0.0189
Mn	0.0150
H	0.0231

Table 6: RMSD (eV/atom) for the prediction of the formation energy (E_{form}) in Rb, Mn, and H single-atom substitutionally defected systems with respect to the non-defected ones.

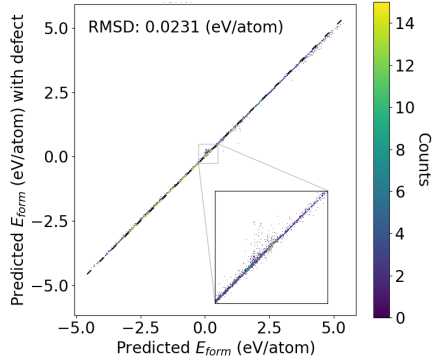


Fig. 4: Predicted formation energy in the H-defected MP crystals with respect to the prediction in non-defected ones. Here only the case of H-defected systems is shown, due to its largest RMSD among the set of considered defects. Similar plots for the Rb and Mn-defected systems are contained in the Supplementary Materials.

one. We focus on pure metallic bulk host matrices, namely Al, Ni, Mo and Au, even though the test could be done on any crystalline matrix. In Fig.(5), we show the key aspects of the performed calculation, with the supercell shown on the left (a), and the elements considered on the right (b). The compositional space considered for the single-atom substitution covers almost the entire periodic table, and also comprises the species highlighted as host matrices when they are not selected as such. Even though our focus is on simple systems, the process can be insightful on the capabilities of the model to learn and predict, with minimal input, physio-chemical trends throughout the periodic table.

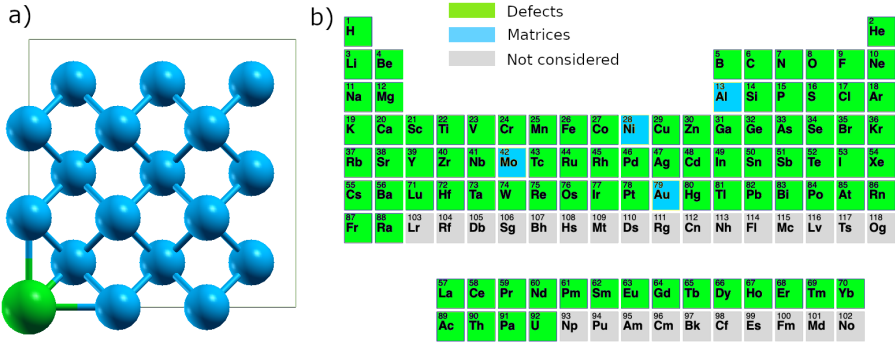


Fig. 5: Periodic table plot (b) explaining the process of selecting a set of host matrices (in light blue) and substitutional defects (in green). To a given a selected host matrix, the non-selected ones represent defects too. The host matrices are $3 \times 3 \times 3$ supercells of the highlighted species (a).

We show periodic table plots for the properties of interest, K_{VRH} , G_{VRH} and E_{form} , for the host matrix which displays the largest deviations in the properties, this is the case of Mo, but analogous plots for the other matrices are included in the Supplementary Material (SM). With the help of the visualization style, we characterize the predictions of the effect on the chemical distance between the substitutional defects and the host matrix on the properties of interest, and how it correlates with the well known trends along the periodic table. In Fig.(6), we show the prediction of the host supercell bulk modulus variation when defected with one of the elements from the periodic table. In particular, in the plot we refer to

$$K'_{\text{VRH}} = K_{\text{VRH}}^{\text{Mo}(X)} - K_{\text{VRH}}^{\text{Mo}} \quad (5)$$

where $K_{\text{VRH}}^{\text{Mo}(X)}$ is the bulk modulus of the Mo matrix defected by atom X, and $K_{\text{VRH}}^{\text{Mo}}$ its value for pure Mo (labelled with a red flag in the figure).

Even though Sr represents an outstanding outlier in decreasing the bulk modulus of the Mo crystal, at this scale it is still possible to appreciate how the

variation happens along the periods: for the 3d, 4d and 5d transition metals from 3rd to 12th group, the defect-induced variations are mainly small, while a tendency to increase is observed, in modulus, in the post-transition metals and, remarkably, in the alkali and alkaline-earth. This behaviour can be interpreted in terms of the well known variations of the bulk modulus along the periodic table of elements, which seem correlated with respect to the defect-induced ones contained in this plot. The effect of substitutional alloying species which, in their bulk and standard temperature and pressure (STP) conditions, show a lower bulk modulus, is, as a tendency, to lower the bulk modulus of their host system.

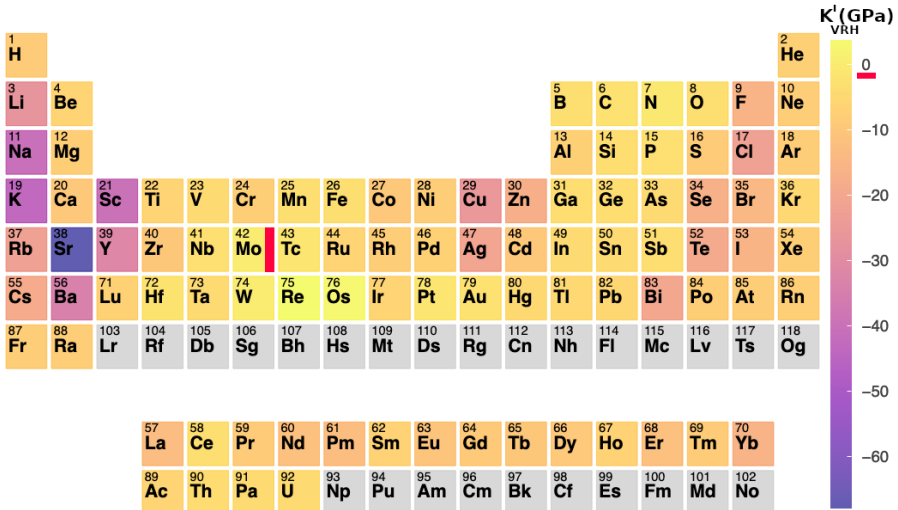


Fig. 6: Predicted bulk modulus variation (K'_{VRH}) for a single-atom substitutionally defected Mo supercell with respect to the undefected one, for each possible defect atomic specie from the provided periodic table. Similar plots for Al, Au and Ni supercells are provided in the Supplementary Materials. The red flag highlights the zero relative difference, meaning the pure Mo matrix selection.

Due to the strong effect induced by the Sr defect, we further focus on transition metals to evaluate how defect-induced variations fluctuate in the

compositional vicinity of the host matrix. Fig.(7) shows the results along the list of 3d, 4d and 5d transition elements, where the variations are harder to distinguish from the prior periodic table plot. We can recognize a decreasing trend that is supportive of our interpretation, but in the compositional vicinity of the host matrix the fluctuations in the defect-induced variations are comparable with the MAE on bulk moduli prediction, just as the differences between the curves.

However, in view of a trend analysis of the variations along the periodic table, Alkali (like K), Alkaline-earth (like Sr and Ba) and post-transition metals (like Se and Te), can support the given interpretation in terms of correlation with the bulk modulus of the impurity, given their associated fluctuations are much larger than the model predictions errors.

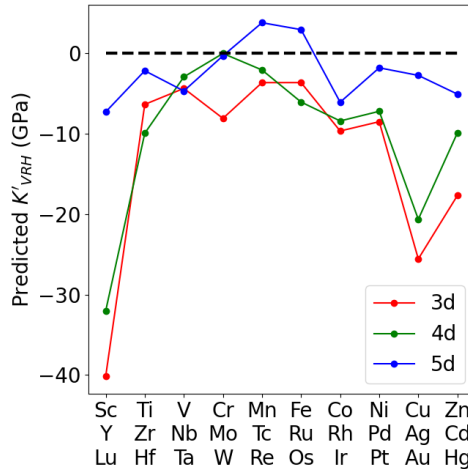


Fig. 7: Predicted bulk modulus variation (K'_{VRH}) for a single-atom substitutionally defected Mo supercell with respect to the undefected one, along the 3d, 4d and 5d series of the periodic table. The black dashed line highlights the pure Mo case.

We may perform analogous investigations for the shear modulus of a pure host matrix, like Mo, and how it gets influenced by single-atom substitutional alloying, spanning over almost the entire periodic table, as shown in Fig.(8). We follow the same protocol and consider the variation $G'_{\text{VRH}} = G_{\text{VRH}}^{\text{Mo}(X)} - G_{\text{VRH}}^{\text{Mo}}$. In this case, the colormap reveals Si as an outlier towards hardening of the Mo matrix. This is a feature that cannot be explained by a correlation in defect- and defect-induced properties trends, since the predicted value is larger than the model prediction error on the shear modulus. We believe that the power of this investigation method is in paving the way to an efficient exploration of substitutional alloying, with the twofold possibility of looking for comparable performances (discovery of alternatives) or outstanding ones (discovery of exceptionals). Similarly to the investigation of the bulk modulus, the Alkali and Alkaline-earth metals like K, Rb, Sr and Ba are among the substitutional species providing the largest decreases in the shear modulus.

Overall, the effects and fluctuations caused by the substitutional defects on the defected host can always be highlighted, but it is not the aim of this work to find an exhaustive explanation for the existing predictions: The reasons for such trends may be due to any of the input parameters, such as the atomic number and bond lengths, or an abstract notion of local environment which is good enough to show reasonable correlations with existing alternative descriptors (i.e. atomic properties). The variations along the 3d, 4d and 5d transition metals are, for most of the cases, below the model MAE for G_{VRH} predictions, therefore no meaningful extrapolation is possible, but we report the plot in Fig.(B9) of the Appendix.

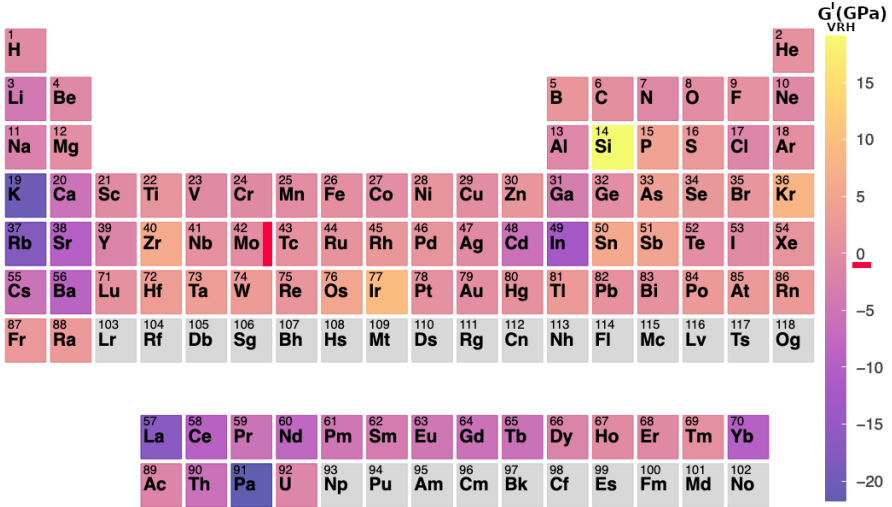


Fig. 8: Predicted shear modulus variation (G'_{VRH}) for a single-atom substitutionally defected Mo supercell with respect to the undefected one, for each possible defect atomic specie from the provided periodic table. Similar plots for Al, Au and Ni supercells are provided in the Supplementary Materials. The red flag highlights the zero relative difference, meaning the pure Mo matrix selection.

For what concerns the formation energy, by definition of the latter, the results in Fig.(9) can be interpreted as the gain or loss in stability after the single-atom substitutional alloying has taken place. Fluorine represents a strong outlier, raising the formation energy by 0.14 eV/atom with respect to the pure Mo matrix. As shown in Fig.(10), it is evident that there is a trend that spans over the periods, and an overall interesting correlation could be found with the known trends for the atomic electronegativity along the periodic table, suggesting that the higher the latter for the substitutional defect in the Mo matrix, the higher is the resulting formation energy.

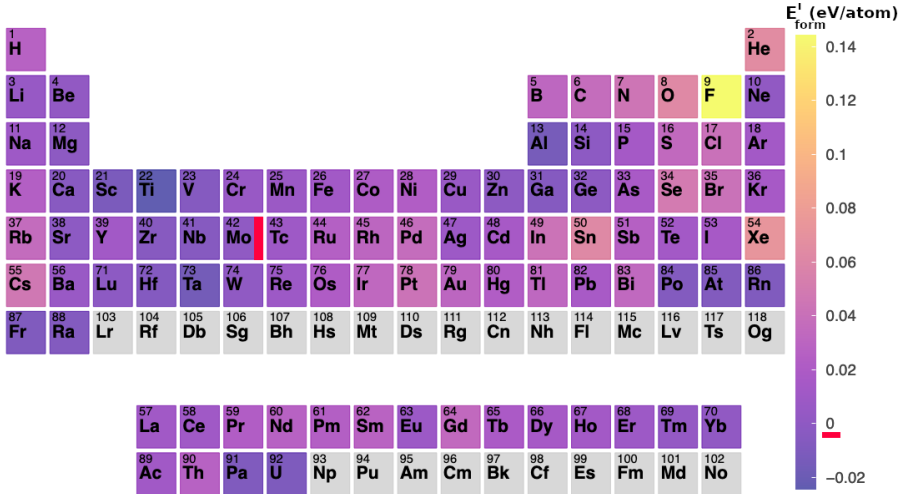


Fig. 9: Predicted formation energy variation (E'_{form}) for a single-atom substitutionally defected Mo supercell with respect to the undefected one, for each possible defect atomic specie from the provided periodic table. Similar plots for Al, Au and Ni supercells are provided in the Supplementary Materials. The red flag highlights the zero relative difference, meaning the pure Mo matrix selection.

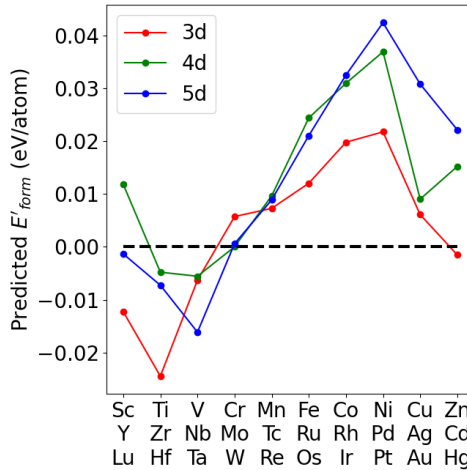


Fig. 10: Predicted formation energy variation (E'_{form}) for a single-atom substitutionally defected Mo supercell with respect to the undefected one, along the 3d, 4d and 5d series of the periodic table. The black dashed line highlights the pure Mo case.

3.3 Property prediction - DFT validation

The validation of artificial intelligence methods predictions is a crucial step in order to quantify their quality. Even though the proposed graph network based method has been already validated for its predictions in bulk crystals, this work aims at testing its capabilities in the presence of single-atom substitutional defects. As explained in Sec.2.2, we compare the model predictions of K_{VRH} , G_{VRH} and E_{form} with the DFT based ones, obtained with the `THERMO_PW` driver of QE. Table(7) shows the results for the validation on the properties in the case of an Al matrix and single-atom substitutional defects, including B, C, I, Ni and Zr.

Comparing the MAE values of our DFT calculations, with the ones of the model for non-defected systems in Table(2), we find good performances of the

System	Method	K_{VRH} (GPa)	G_{VRH} (GPa)	E_{form} (eV/atom)
Al _B	MEGNet	84.456	60.405	0.050
	DFT	78.101	24.074	0.096
Al _C	MEGNet	87.165	34.762	0.113
	DFT	73.791	16.673	0.228
Al _I	MEGNet	72.697	29.796	0.056
	DFT	63.655	13.514	0.475
Al _{Ni}	MEGNet	84.683	30.437	0.009
	DFT	81.363	37.086	4.567
Al _{Zr}	MEGNet	87.881	29.158	-0.048
	DFT	79.672	30.068	1.262
MAE		8.060	15.653	1.290

Table 7: Comparison of the DFT and MEGNet results for the three properties of interest in a small set of samples. Here, Al_B means a single B-atom substitution in an Al host $2 \times 2 \times 2$ supercell matrix.

model with respect to K_{VRH} and G_{VRH} predictions, but large errors when it comes to the formation energies: the first may be regarded as a success, given that the model is predicting properties of a new class of systems, and given the computational limitations; the second one is a negative signature, even though the (i) defect dependent nature of the error order of magnitude opens up a deeper window of investigation on its reasons, and (ii) the validation set for defected systems is extremely small compared to the undefected MP dataset, on which initial MAEs have been evaluated.

3.4 Size effects

In substitutional alloying, the defect atomic specie is usually present in a dilute concentration, in the range of 0.1-10%. For this reason, it is of interest the study of how the property predictions vary with defect concentration, that we propose in the saturation plots of Fig.(11), Fig.(12) and Fig.(13). Our example system follows the choice of the Mo host matrix, with the H, Mn and Rb substitutional defects we focused on, respectively in the second and first part of the previously reported results. Interestingly, a hierarchy is conserved among the defect-induced variations for different host supercell sizes: the single Rb defect always causes the largest deviations of the studied properties from their

asymptotic over-dilute level ($< 0.1\%$). Moreover, while the defect formation energy, as expected, shows a common descent to zero-level for all the defect species, the predicted structural properties seem to be sensitive on them, with the Rb-defected Mo crystal conserving a visible difference in the property value even at the limit of 0.1% concentration, both for K_{VRH} and G_{VRH} . Even though it is out of the present work aims to validate the asymptotic-size behaviour of the predictions with accurate but expensive DFT calculations, we believe these results to stand in favour of the positive model understanding of a crystalline defected system environment.

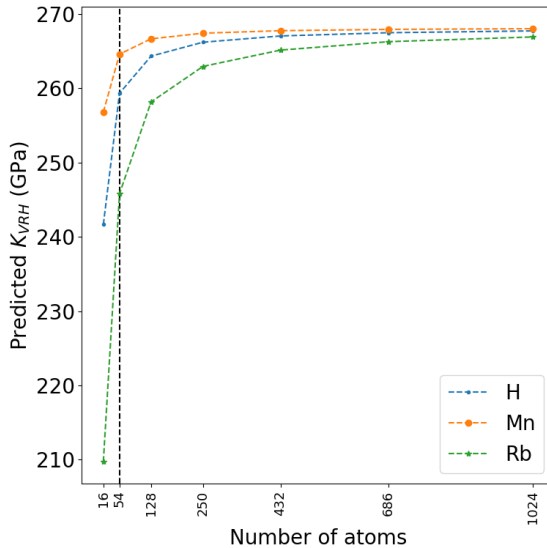


Fig. 11: Saturation plot of a Mo host matrix K_{VRH} when substitutionally defected with H, Mn or Rb, for different supercell sizes.

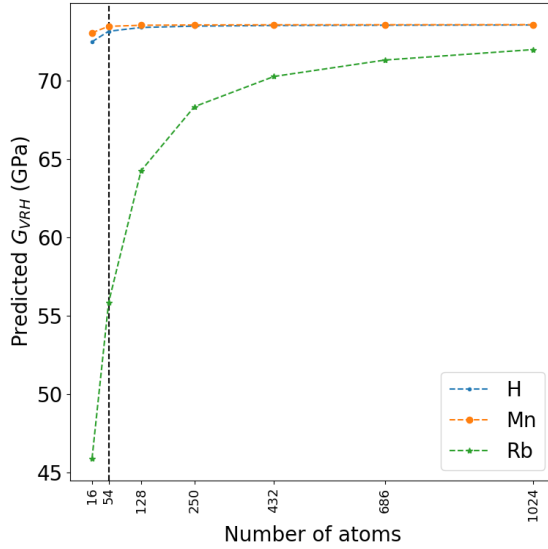


Fig. 12: Saturation plot of a Mo host matrix G_{VRH} when substitutionally defected with H, Mn or Rb, for different supercell sizes.

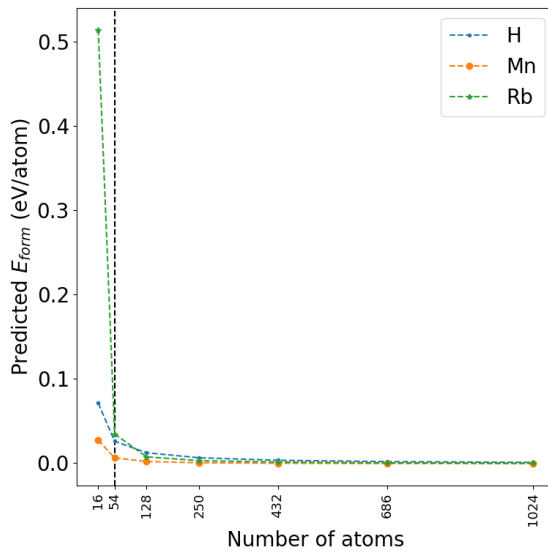


Fig. 13: Saturation plot of a Mo host matrix E_{form} when substitutionally defected with H, Mn or Rb, for different supercell sizes.

Let us continue along the previously paved path of analysis which also looks into the effects of systematically changing the substitutional atomic specie among the large variety contained in the periodic table, as previously done in Fig.(6), with the only exception of selecting the smallest and largest supercell sizes from the previous saturation plots of Fig.(11), respectively $2 \times 2 \times 2$ (1% concentration, 16 atoms cell) and $8 \times 8 \times 8$ (10% concentration, 1024 atoms cell). In Fig.(14), focusing on the first row of plots which deal with the K'_{VRH} variation, and comparing with the previously investigated supercell case of size $3 \times 3 \times 3$ (2% concentration) of Fig.(6), one can notice that the scale of property variations changes accordingly: smaller defect concentrations lead to smaller defect-induced effects, and viceversa, as expected. In particular, in the largest supercell case the induced variations range is reduced to a 3% of the $3 \times 3 \times 3$ system's one. However, the composition map outliers are left unchanged. The shear modulus variations, in the second row of tables, sees the emergence of new outliers in the chemical neighbourhoods of the previously obtained ones in $3 \times 3 \times 3$ supercells, while the formation energy variations undergo both a change in scale and a complete change in the map outliers. Following the brief assessment of predictions quality performed for each of the interesting properties in the previous section, we expect the formation energy variations to suffer by non-negligible fluctuations, leading to the possible need of further validation. However, the main aim of the present discussion is to underline the power of the overall approach in highlighting the path towards composition search in substitutional alloying, which can effectively drive to specific desired emerging properties.

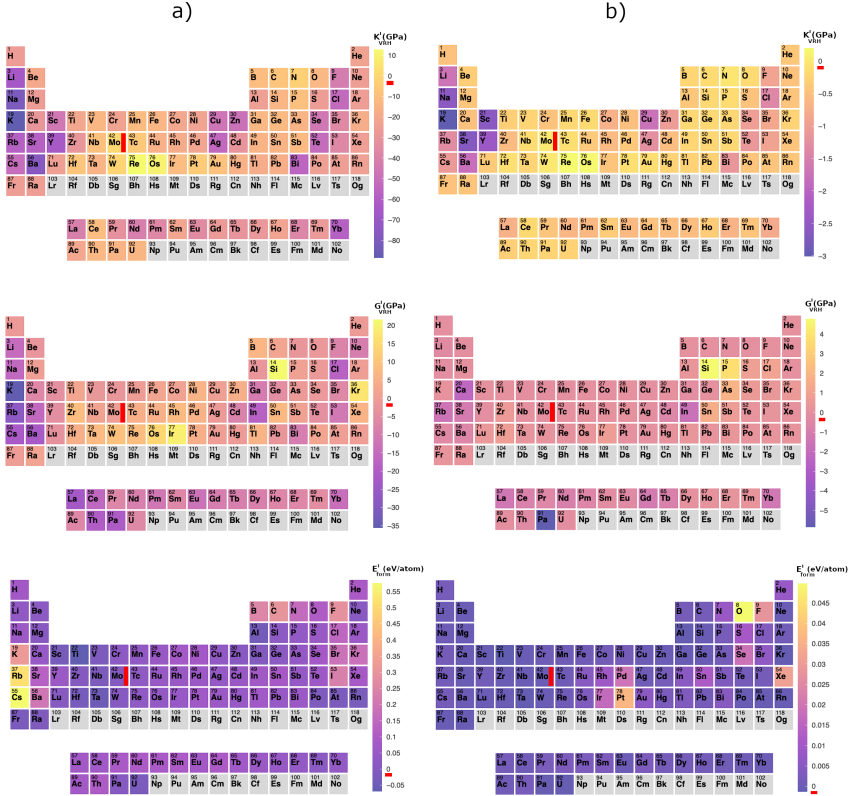


Fig. 14: Predicted variations K'_{VRH} (first row plots), G'_{VRH} (second row plots), E'_{form} (third row plots) for a single-atom substitutionally defected Mo supercell with respect to the undefected one, for each possible defect atomic specie from the provided periodic table. In plots of column a) a $2 \times 2 \times 2$ supercell is considered, while in column b) a $8 \times 8 \times 8$ supercell.

4 Conclusions

In this work, we utilized a convolutional graph-neural network, based on the MEGNet architecture [Chen et al \(2022\)](#), in order to attempt the design of novel alloys. Alloying involves substitutional and interstitial alloying at relatively low concentrations, thus, single-defect properties shall be informative on overall designing capabilities and guidance. For this purpose, we utilized the MP database, and we focused on the prediction of the properties of single-atom

substitutionally defected bulk crystals, in the context of both (i) systematic substitution with a specific set of species in a wide variety of crystals from the entire Materials Project dataset and (ii) systematic substitution with a variety of atomic species in a specific set of pure bulk crystals. We also validated some of the results with our own DFT calculations. We believe that such approaches might provide novel insights into alloy design, especially if predictions include extended lattice defects such as dislocations and/or grain boundaries.

Acknowledgments. We would like to thank J. Llorca for insights and fruitful discussions and suggestions. This research was funded in part by the European Union Horizon 2020 research and innovation program under Grant Agreement No. 857470 and from the European Regional Development Fund via Foundation for Polish Science International Research Agenda PLUS program Grant No. MAB PLUS/2018/8.

4.1 Data availability

Requests for additional data and availability can be directed to the provided lead contact. The employed DFT data, ML model and database can be found on the GitHub: <https://github.com/danielcieslinski/suballoy>

Declarations

Declarations

References

Back S, et al (2019) Convolutional neural network of atomic surface structures to predict binding energies for high-throughput screening of catalysts. *J Phys Chem Lett* 10:4401–4408

- Balachandran PV, et al (2018) Predictions of new abo₃ perovskite compounds by combining machine learning and density functional theory. *Phys Rev Mater* 2(1-18)
- Behler J (2011) Atom-centered symmetry functions for constructing high-dimensional neural network potentials. *J Chem Phys* 134(074106)
- Chen C, et al (2019a) Graph networks as a universal machine learning framework for molecules and crystals. *Chem Mater* 31(9):3564
- Chen C, et al (2019b) Graph networks as a universal machine learning framework for molecules and crystals. *Chem Mat* 31:3564–3572
- Chen C, et al (2022) The megnet model on github. URL <https://github.com/materialsvirtuallab/megnet/blob/master/megnet/models/megnet.py>
- Coley CW, et al (2017) Convolutional embedding of attributed molecular graphs for physical property prediction. *J Chem Info Model* 57(1757-1772)
- Curtarolo S (2012) A distributed materials properties repository from high-throughput ab initio calculations. *Comput Mater Sci* 58(227)
- Curtarolo S, et al (2013) The high-throughput highway to computational materials design. *Nat Mater* 12:191
- Dal Corso A (2023) https://dalcorsi.github.io/thermo_pw/
- De S, et al (2016) Comparing molecules and solids across structural and alchemical space. *Phys Chem Chem Phys* 18:13,754–13,769
- Deml A, et al (2014) Oxide enthalpy of formation and band gap energy as accurate descriptors of oxygen vacancy formation energetics. *Energy Environ*

Sci 7(1996)

Deml A, et al (2015) Intrinsic material properties dictating oxygen vacancy formation energetics in metal oxides. *J Phys Chem Lett* 6(1948)

Dunn A, et al (2020) Benchmarking materials property prediction methods: the matbench test set and automatminer reference algorithm. *Npj Comput Mater* 6:138

Duvenaud DK, Maclaurin D, Iparraguirre J, et al (2015) Convolutional networks on graphs for learning molecular fingerprints. *Advances in neural information processing systems* 28

Fung V, et al (2021) Benchmarking graph neural networks for materials chemistry. *Npj Comput Mat* 7(84)

Giannozzi P, et al (2009) *JPhys: CondensMatter* 21(39550)

Giannozzi P, et al (2017) *JPhys: CondensMatter* 29(465901)

Giannozzi P, et al (2020) *J Chem Phys* 152(154105)

Gong W, Yan Q (2021) Graph-based deep learning frameworks for molecules and solid-state materials. *Computational Materials Science* 195:110,332

Gu GH, et al (2020) Practical deep-learning representation for fast heterogeneous catalyst screening. *J Phys Chem Lett* 11:3185–3191

Guan Z (2019) Compositional engineering of multinary cu–in–zn-based semiconductor nanocrystals for efficient and solution-processed red-emitting quantum-dot light-emitting diodes. *Org Electron* 74(46)

- Hachmann J, et al (2011) The harvard clean energy project: Large-scale computational screening and design of organic photovoltaics on the world community grid. *J Phys Chem Lett* 2(2241)
- Isayev O, et al (2017) Universal fragment descriptors for predicting properties of inorganic crystals. *Nat Commun* 8(15679)
- Jain A, et al (2013) The materials project: A materials genome approach to accelerating materials innovation. *APL Mater* 1(011002)
- Jorgensen J, et al (2018) Neural message passing with edge updates for predicting properties of molecules and materials. arXivorg e-Print archive p arXiv:1806.01261
- Karamad M, et al (2020) Orbital graph convolutional neural network for material property prediction. *Phys Rev Mater* 4:093,801
- Kaxiras E (2003) *Atomic and Electronic Structure of Solids*. Cambridge University Press
- Kearnes S, et al (2016) Molecular graph convolutions: Moving beyond fingerprints. *J Comput-Aided Mol Des* 30(595–608)
- Klug M, et al (2017) Tailoring metal halide perovskites through metal substitution: influence on photovoltaic and material properties. *Energy Environ Sci* 10(236)
- L. Ward CW (2017) Atomistic calculations and materials informatics: A review. *Current Opinion in Solid State and Materials Science* 21(3)
- LeCun Y, et al (2015) Deep learning. *Nature* 521:436

- Liu Y, et al (2019) High-throughput experiments facilitate materials innovation: a review. *Science China Technological Sciences* 62:521–545
- Louis SY, et al (2020a) Graph convolutional neural networks with global attention for improved materials property prediction. *Phys Chem Chem Phys* 22:18,141–18,148
- Louis SY, et al (2020b) Graph convolutional neural networks with global attention for improved materials property prediction. *PhysChemChemPhys* 22:18,141
- Mannodi-Kanakkithodi A, et al (2020) Machine-learned impurity level prediction for semiconductors: the example of cd-based chalcogenides. *NPJ Comput Mater* 6(1)
- Mannodi-Kanakkithodi A, et al (2022) Universal machine learning framework for defect predictions in zinc blende semiconductors. *Patterns* 3(100450)
- Methfessel M, Paxton AT (1989) *Phys Rev B* 40(3616)
- Michalski RS, et al (2013) Machine learning an artificial intelligence approach. Springer Science and Business Media
- Ning CZ, et al (2017) Bandgap engineering in semiconductor alloy nanomaterials with widely tunable compositions. *Nat Rev Mater* 2(1)
- NOMAD (<https://nomad-coe.eu>)
- Oba F, et al (2018) Design and exploration of semiconductors from first principles: a review of recent advances. *Appl Phys Express* 11(060101)

- Ong SP, et al (2013) Python materials genomics (pymatgen): A robust, open-source python library for materials analysis. *Comput Mater Sci* 68(314)
- Palizhati A, et al (2019) Toward predicting inter-metallics surface properties with high-throughput dft and convolutional neural networks. *J Chem Inf Model* 59:4742–4749
- Park CW, Wolverton C (2020a) Developing an improved crystal graph convolutional neural network framework for accelerated materials discovery. *Phys Rev Mater* 4:063,801
- Park CW, Wolverton C (2020b) Developing an improved crystal graph convolutional neural network framework for accelerated materials discovery. *Phys Rev Mater* 4:063,801
- Perdew JP, et al (1996) *Phys Rev Lett* 77(3865)
- Pietrucci F, Andreoni W (2011) Graph theory meets ab initio molecular dynamics: Atomic structures and transformations at the nanoscale. *Phys Rev Lett* 107(085504)
- Rajan K (2005) Materials informatics. *Materials Today* 8(10):38–45
- Ramakrishna S, et al (2019) Material informatics. *J Intell Manuf* 30:2307–2326
- Ramprasad R, et al (2017) Machine learning in materials informatics: recent applications and prospects. *Npj Comput Mater* 3(54)
- Reiser P, et al (2022) Graph neural networks for materials science and chemistry. *Communications Materials* 3:93

- Rupp M, et al (2012) Fast and accurate modeling of molecular atomization energies with machine learning. *Phys Rev Lett* 108(058301)
- Saal E, et al (2013) Materials design and discovery with high-throughput density functional theory: The open quantum materials database (oqmd). *JOM* 65(1501)
- Sadeghi A, et al (2013) Metrics for measuring distances in configuration spaces. *J Chem Phys* 139(184118)
- Sampson M, et al (2017) Transition metal-substituted lead halide perovskite absorbers. *J Mater Chem A* 5(3578)
- Schütt K, Kindermans PJ, Saucedo Felix HE, et al (2017) Schnet: A continuous-filter convolutional neural network for modeling quantum interactions. *Advances in neural information processing systems* 30
- Seko A, et al (2015) Prediction of low-thermal-conductivity compounds with first-principles anharmonic lattice-dynamics calculations and bayesian optimization. *Phys Rev Lett* 115:205,901
- Sharma V, et al (2020) Machine learning substitutional defect formation energies in ABO_3 perovskites featured. *Journal of Applied Physics* 128(034902)
- Takahashi K, Tanaka Y (2016) Materials informatics: a journey towards material design and synthesis. *Dalton Trans* 45:10,497–10,499
- Varley J, et al (2017) Descriptor-based approach for the prediction of cation vacancy formation energies and transition levels. *J Phys Chem Lett* 8(5059)
- Wan Z, et al (2021) Data-driven machine learning model for the prediction of oxygen vacancy formation energy of metal oxide materials. *Phys Chem*

Chem Phys 23(15675)

Wu Z, Ramsundar B, Feinberg EN, et al (2018) Moleculenet: a benchmark for molecular machine learning. *Chemical science* 9(2):513–530

Wu Z, et al (2021) A comprehensive survey on graph neural networks. *IEEE Trans Neural Netw Learn Syst* 32:4–24

Xie T, Grossman JC (2018a) Crystal graph convolutional neural networks for an accurate and interpretable prediction of material properties. *Phys Rev Lett* 120:145,301

Xie T, Grossman JC (2018b) Hierarchical visualization of materials space with graph convolutional neural networks. *J Chem Phys* 149:174,111

Xue D, et al (2016) Accelerated search for materials with targeted properties by adaptive design. *Nat Commun* 7 7(11241)

Ye W, et al (2018) Deep neural networks for accurate predictions of crystal stability. *Nat Commun* 9(1-6)

Zhai X, et al (2022) Predicting the formation of fractionally doped perovskite oxides by a function-confined machine learning method. *Commun Mater* 3(42)

Zhou J, et al (2020) Graph neural networks: a review of methods and applications. *AI Open* 1:57–81

Appendix A Further Results for: Property prediction - A defect in a wide range of matrices

As mentioned in Sec.(3.2), we first focus on the prediction of defected systems properties, when the systematic substitutional defective process is applied with the same atom on the Materials Project crystals dataset. There, we show the RMSD for the predictions of bulk modulus, shear modulus, and defect formation energy, respectively in Fig.(2) and Table(4), Fig.(3) and Table(5), and Fig.(4) and Table(6). However, the figures are there reported only for the defects leading to the corresponding largest RMSD values. Here, for completeness, we report the missing ones in Fig.(A1), Fig(A2) and Fig(A3).

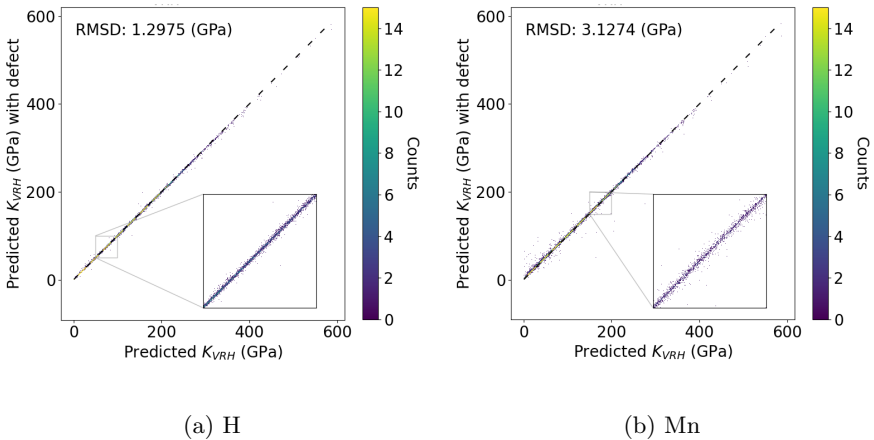


Fig. A1: Predicted bulk modulus in the H- and Mn-defected MP crystals with respect to its prediction in non-defected ones.

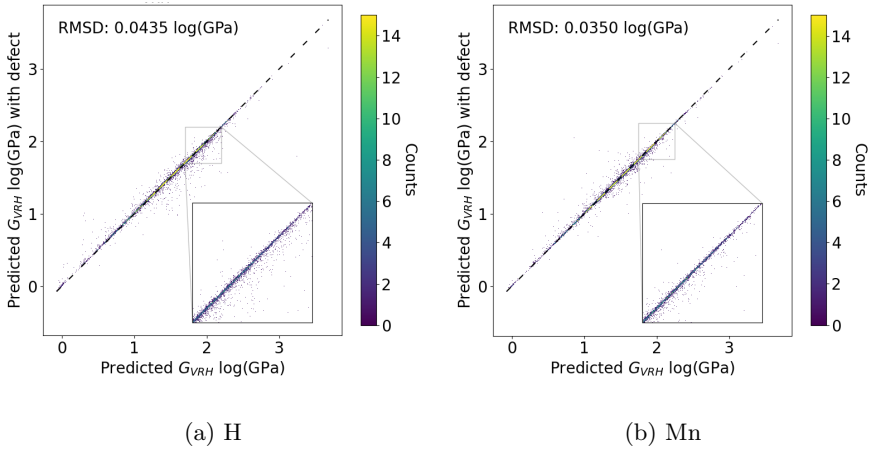


Fig. A2: Predicted shear modulus in the H- and Mn-defected MP crystals with respect to its prediction in non-defected ones.

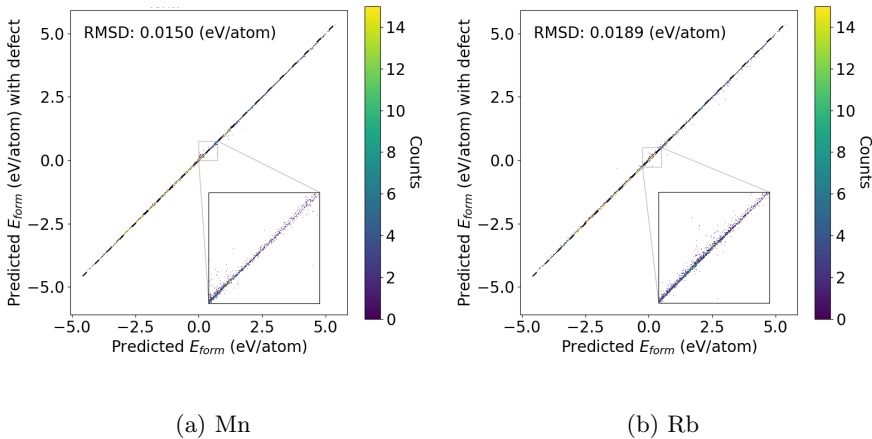


Fig. A3: Predicted formation energy in the Mn- and Rb-defected MP crystals with respect to its prediction in non-defected ones.

For the shear modulus predictions, the reader might have noticed the choice of a different scale for the plots. A part from noticing a common use in the

literature of the log-log scale for this quantity and adopting the same for the sake of comparison, we also decided to understand the reason behind this choice by plotting in a normal scale as in Fig.(A4): the wide scale over which few predictions are spreading does not allow to appreciate the distribution of the data.

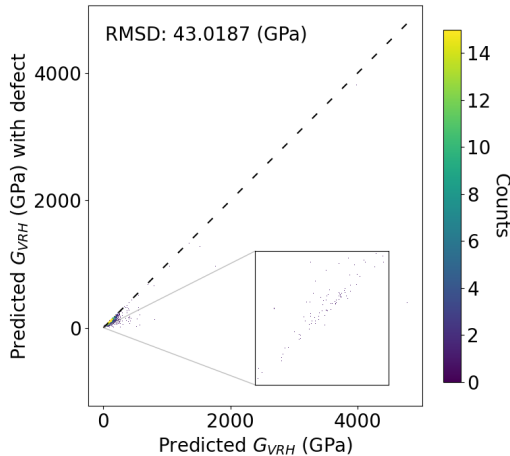


Fig. A4: Predicted formation energy in the Rb-defected MP crystals with respect to its prediction in non-defected ones. The plot has the aim to display the need of a log-log scale to appreciate the deviations.

Appendix B Further Results for: Property prediction - A wide range of defects in the same matrix

Following a similar selection criterion for the results to which the main body of the manuscript is dedicated, for the second part of our investigation, in which we consider the systematically change of the single-atom substitutional defect specie in the same crystal structure, we decided to show the results

for the Molybdenum host matrix, which was displaying, overall, the largest variations in the interesting quantities. In Fig.(B5) and Fig.(B6), we report the collection of defect-induced variations in the bulk modulus, shear modulus, and formation energy for the all host-matrices investigated here, respectively Ni and Mo, and Au and Al. A composite visualization of all the variational periodic tables allows for an overall comparison, and helps in appreciating that interesting effects in the previously not shown matrices are not missing:

- the shear modulus variation scale of the Ni matrix upon single-atom substitution is comparable to the one of Mo, and they also share alkaline and alkaline earth metals in the lower bound variations;
- similarly to the previous point, Au and Al share a similar variation scale and outlier map for the bulk modulus, and, in particular, for the formation energy

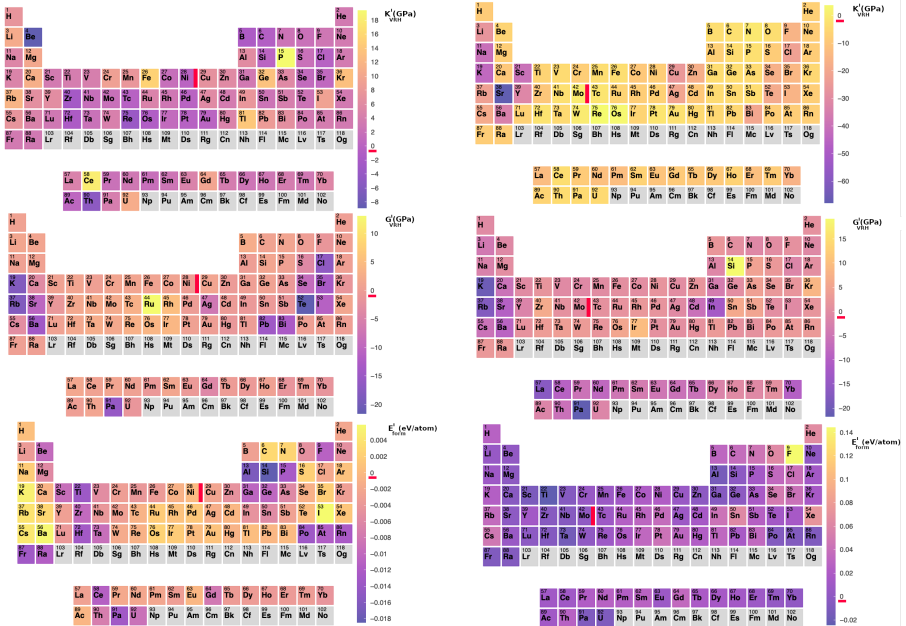


Fig. B5: Comparison between the periodic table plots of the predicted bulk modulus, shear modulus and formation energy for a single-atom substitutionally defected Ni (left column) and Mo (right column) supercell with respect to the undefected one, for each possible atomic specie from the provided periodic table.

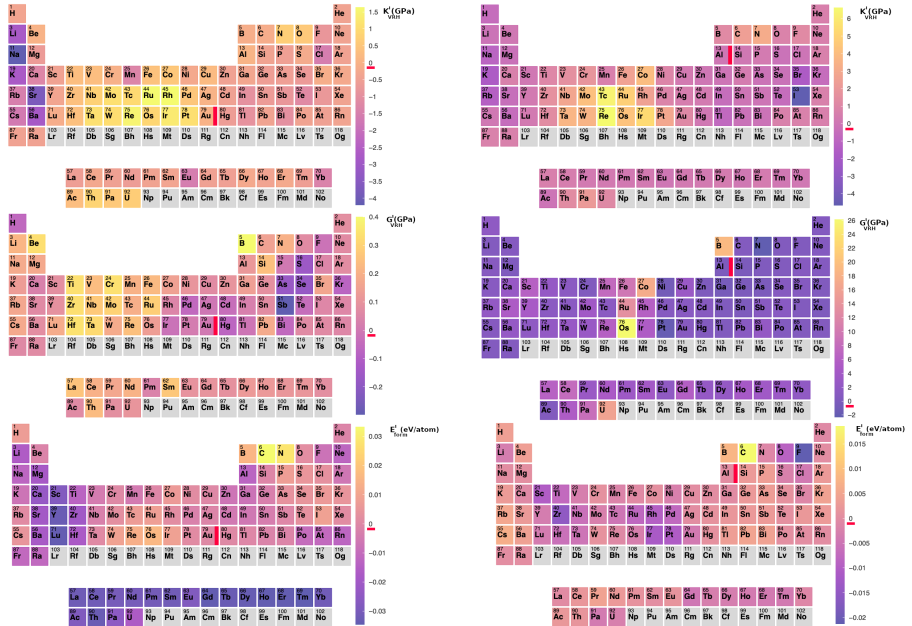


Fig. B6: Comparison between the periodic table plots of the predicted bulk modulus, shear modulus and formation energy for a single-atom substitutionally defected Au (left column) and Al (right column) supercell with respect to the undefected one, for each possible atomic specie from the provided table.

Even though the variations in the interesting properties upon substitutional-defecting of the host matrices are dominant for the Mo matrix, we here want to report, as previously done, all the variations, and draw a brief comparison between them in a combined visualization. While the trends in the bulk modulus variations of Mo and Ni matrices are noticeably different, Al and Au show pretty similar trends and hierarchies on different scales: the central 4d and 5d elements tend to maximize the variations, with a minimization happening at extremas and, for both, for a Mn substitution. In particular, it is interesting to notice that in the Al matrix nearly all the periodic table elements considered lead to a positive bulk modulus variation. A similarity between variations in Mo and Ni holds for the shear modulus variations, which

share comparable scales and a similar exchanged role of 5d (in Mo) and 4d (in Ni) substitutions, and for the formation energy variations, showing remarkably similar trends over scales differing by an order of magnitude.

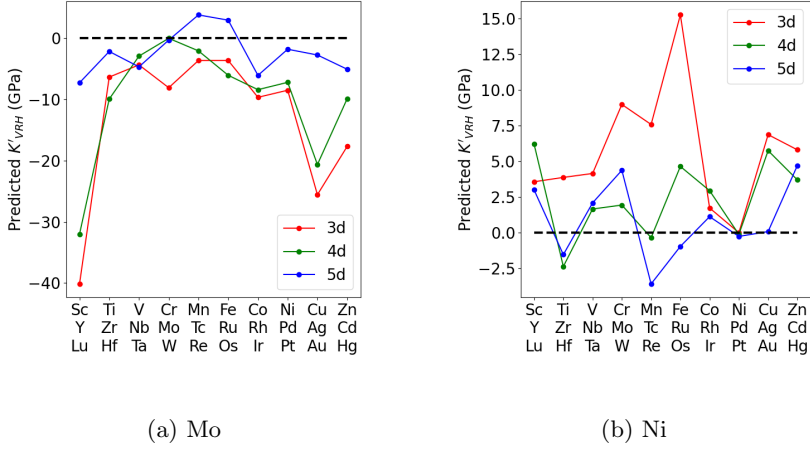
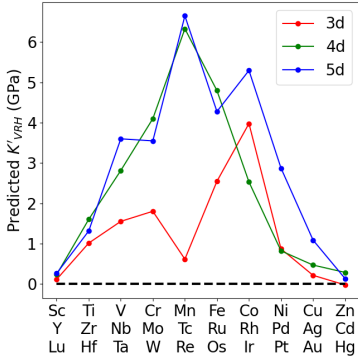
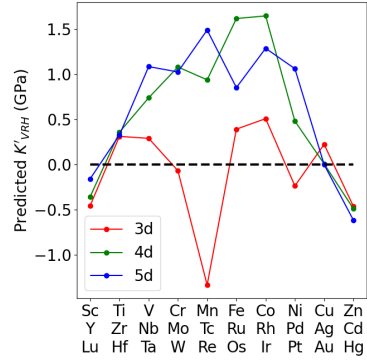


Fig. B7: Predicted bulk modulus variation (K'_{VRH}) for a single-atom substitutionally defected Mo and Ni supercell with respect to the undefected one, along the 3d, 4d and 5d series of the periodic table. The black dashed line highlights the pure host matrix case.

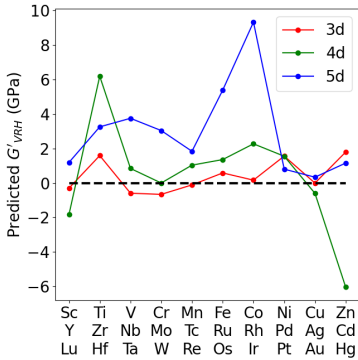


(a) Al

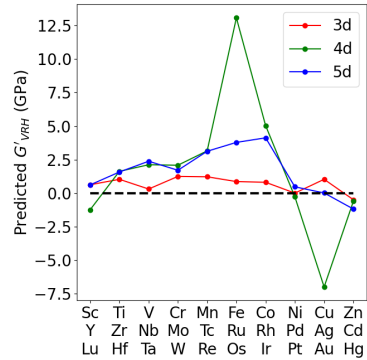


(b) Au

Fig. B8: Predicted bulk modulus variation (K'_{VRH}) for a single-atom substitutionally defected Al and Au supercell with respect to the undefected one, along the 3d, 4d and 5d series of the periodic table. The black dashed line highlights the pure host matrix case.



(a) Mo



(b) Ni

Fig. B9: Predicted shear modulus variation (G'_{VRH}) for a single-atom substitutionally defected Mo and Ni supercell with respect to the undefected one, along the 3d, 4d and 5d series of the periodic table. The black dashed line highlights the pure host matrix case.

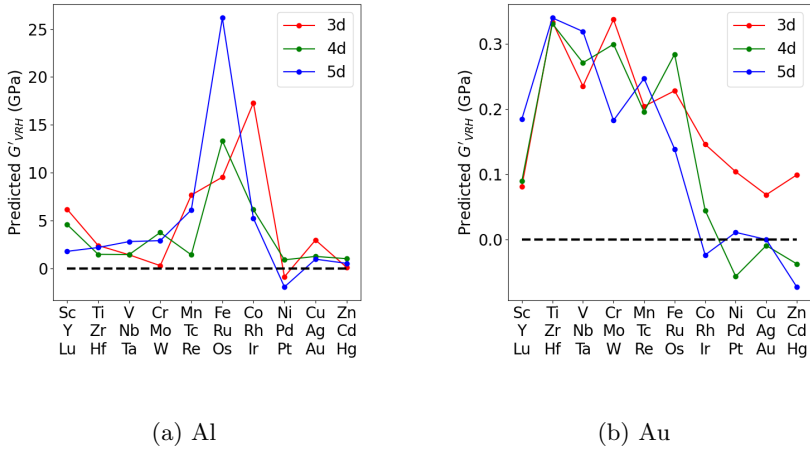


Fig. B10: Predicted shear modulus variation (G'_{VRH}) for a single-atom substitutionally defected Al and Au supercell with respect to the undefected one, along the 3d, 4d and 5d series of the periodic table. The black dashed line highlights the pure host matrix case.

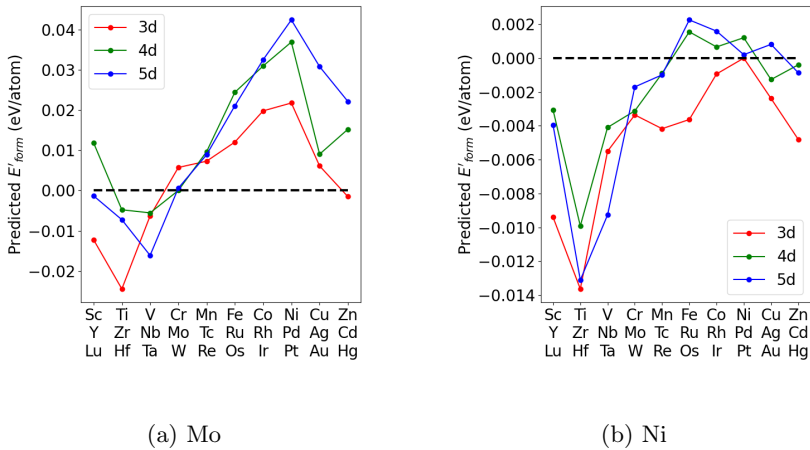
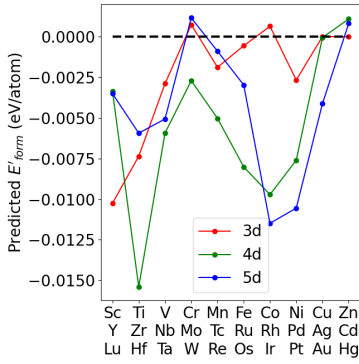
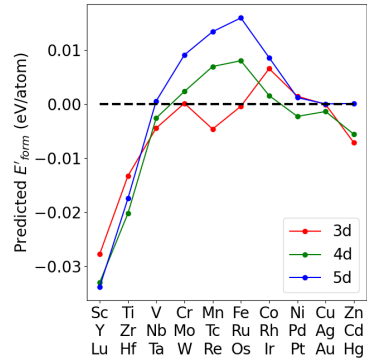


Fig. B11: Predicted formation energy variation (E'_{form}) for a single-atom substitutionally defected Mo and Ni supercell with respect to the undefected one, along the 3d, 4d and 5d series of the periodic table. The black dashed line highlights the pure host matrix case.



(a) Al



(b) Au

Fig. B12: Predicted formation energy variation (E'_{form}) for a single-atom substitutionally defected Al and Au supercell with respect to the undefected one, along the 3d, 4d and 5d series of the periodic table. The black dashed line highlights the pure host matrix case.